Broadband Terahertz Computed Tomography Using a 5k-pixel Real-time THz Camera

2 authors:

Georgios C. Trichopoulos
Arizona State University
54 PUBLICATIONS   **190** CITATIONS

SEE PROFILE

Kubilay Sertel
The Ohio State University
275 PUBLICATIONS   **2,330** CITATIONS

SEE PROFILE

Some of the authors of this publication are also working on these related projects:

Project   Towards 6G: The synergy of mmWave communications, imaging, and localization   View project

Project   UWB mmW array   View project

A Broadband Focal Plane Array Camera for Real-time THz Imaging Applications

Georgios C. Trichopoulos, *Student Member, IEEE*, H. Lee Mosbacker, Don Burdette, and
Kubilay Sertel, *Senior Member, IEEE*

Abstract—We present a large-format, sub-millimeter-resolution, focal plane array sensor for THz imaging. Each pixel in the sensor array consists of broadband THz antennas monolithically integrated with ultra-fast heterostructure backward diodes for THz sensing. With the aid of in-house hybrid electromagnetic modeling tools, the focal plane array is optimized for diffraction limited image resolution and conjugate impedance matching for highest THz sensitivity. The camera is designed to operate in the 0.6–1.2 THz band with 5 frames-per-second image acquisition speeds, making it ideal for THz imaging applications, such as security screening, non-destructive evaluation and chemical, pharmaceutical, and medical imaging. The simulation results are validated by measurements to demonstrate sub-millimeter resolution with a pixel optical responsivity of 600 V/W at 0.7 THz.

Index Terms—Focal plane arrays, heterostructure backward diodes, quasi-optical imaging, tHz imaging.

I. INTRODUCTION

LACK of large-format (many-pixel) sensor arrays is one of the major hurdles for the proliferation of THz sensing methodologies and related applications. Among those, medical imaging and security screening are perhaps the most widely publicized. Imaging modalities in optical and infrared (IR) wavelengths suffer from low penetration depths and are thus not attractive for non-destructive evaluation applications. In contrast, THz waves can penetrate most materials and can provide unique spectral information in the 0.1–10 THz band with high spatial resolution. Moreover, unlike X-ray-based radiological images, frequency sensitivity of THz absorption can help identify differences in biological tissues. The spectroscopic information content of various chemical and biological materials in the THz band has been studied extensively in the recent years [1], particularly in the 30–900 GHz band for medical applications [2]. For example, Ashworth *et al.* [3] conducted excised tissue absorption spectra measurements in the 0.15–2 THz range. Furthermore, some pharmaceutical substances, such as biotin and avidin exhibit absorption spectra in the 0.1–1.2 THz band, a property employed for amplification of bioaffinity detection [4]. In addition, the non-ionizing nature of THz radiation coupled with its sub-millimeter scale resolution and the ability to penetrate typical packaging and clothing materials makes the THz band ideal for standoff screening applications [5], as well as non-invasive inspection of packaged goods and devices.

Albeit the aforementioned potential applications, excessive cost and large sizes of available THz spectroscopy systems hinder the proliferation of this new technology. Many state-of-the-art THz spectroscopy systems rely on ultrafast laser-based systems that are expensive, bulky, and thus non-portable. Moreover, these THz imaging systems typically employ mechanical raster scans (using single detector) to acquire two-dimensional images. As such, this scan process often takes tens of minutes to generate a high-resolution THz picture of a scene. Additionally, such devices tend to be bulky and complicated due to the necessary mechanical parts, and are thus rather expensive to develop and operate. Thus, all-electronics-based THz systems are badly needed to minimize the space, weight and power, and enable future THz sensing and communications systems.

Recent advances in semiconductor material and device technology are paving the way towards all-electronic THz systems. Novel ultrafast electronic devices, such as heterostructure backward diodes can exhibit extremely high cutoff frequencies (~ 8 THz) [6] and 2-D electron gas (2DEG) high electron mobility transistors (HEMTs) are capable of operating at frequencies well above 1 THz [7]. Already, InP based THz transistors [8] have been incorporated into THz monolithic integrated circuits (TMICs), and 0.670 THz communications subsystems have been demonstrated. Additionally, CMOS SOI field effect transistor (FET) detectors have been implemented based on plasma wave excitation [9], [10]. In recent work, a group has built a 32×32 pixel THz FPA based on CMOS technology that operates in the 0.6–1 THz band [11].

These recent developments in new semiconductor materials and device topologies will no doubt enable and fuel new and continuing research in integrated THz systems. Here, we present a new THz focal plane array (FPA) sensor that incorporates ultrafast (2.5 THz intrinsic cut-off frequency), zero-biased, antimonide based heterostructure backward diodes (Sb-HBDs)[6], monolithically integrated with planar THz antennas for each sensor pixel (see Fig. 1). The FPA is situated behind an extended hemispherical lens [12] made of high-resistivity float zone silicon ($\varepsilon_r \sim 11.7$, resistivity > 10 kΩ/cm).

A typical focal plane array (FPA)-based imaging system is illustrated in Fig. 2. Although the optical components (i.e., lenses)
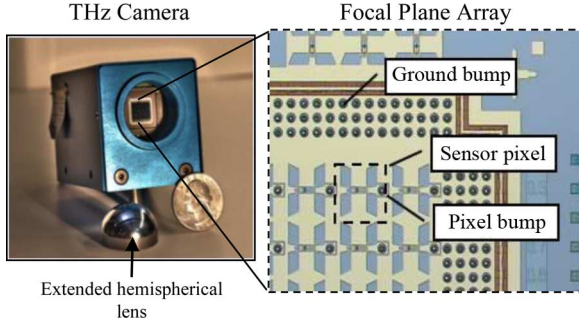
Fig. 1. Photograph of the THz camera developed at the Ohio State University. Left: camera housing with the hemispherical lens removed. Right: microscope image illustrating the details of the focal plane array pixels consisting of broadband slot antennas with integrated sensors.
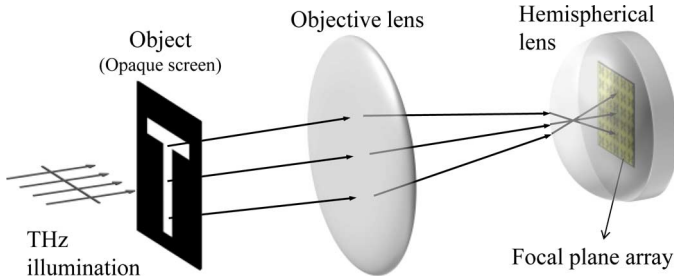

Fig. 2. "Reverse microscope" configuration for THz FPA imaging: Terahertz radiation emanating from the object plane is collected by the optical components (e.g., the objective lens as shown). The hemispherical lens is used to focus the image on the FPA sensor. Subsequently, an electronic read-out digitizes the baseband signal from each pixel and forms a digital image.

of this setup is reminiscent of commercial optical digital cameras, the THz FPA sensor is quite different from CMOS- or CCD-based sensors that are typically used in optical or infrared sensing. Due to the much longer wavelengths (compared to optical and IR) and much lower energies of THz waves, the pixels in a THz FPA consist of antenna structures that capture and direct the incoming THz radiation onto the non-linear semiconductor sensor device. Planar slot antennas (shown in Fig. 3) residing on the focal plane of an extended hemispherical lens are used for coupling THz energy emanating from the object, since their radiation and reception is primarily ($\sim 95\%$ for $\varepsilon_r \sim 11.7$) directed toward to high permittivity lens/substrate half-space [13]. In essence, these antennas constitute the pixels of the THz FPA sensor that couple the incoming THz energy onto the HBDs (shown in the inset of Fig. 3). Subsequently, the THz signal is rectified to a DC or baseband signal (a.k.a. direct detection) and the diode output signal is collected and digitized by a suitable read-out integrated circuit (ROIC). The electronics multiplex the THz pixel outputs to an intermediate board that digitizes and converts the data to a standard CAMLINK signal compatible with any off-the-shelf frame grabber. We note here that the ROIC hosts 320×256 pixels separated by 25 μm, whereas the FPA consists of 80×64 antennas with 100 μm pitch. As a result only 1 out of 4 ROIC pixels is used for THz imaging.

Compared to heterodyne down-conversion, this simple direct detection scheme allows for densely-packed large-scale arrays since there is no need for bulky and expensive local oscillators (LO) and LO injection circuitry. Also, large IF filters for signal recovery are avoided. However, this direct detection approach cannot capture the signal's phase information and the overall sensitivity is significantly lower than heterodyne detection. In
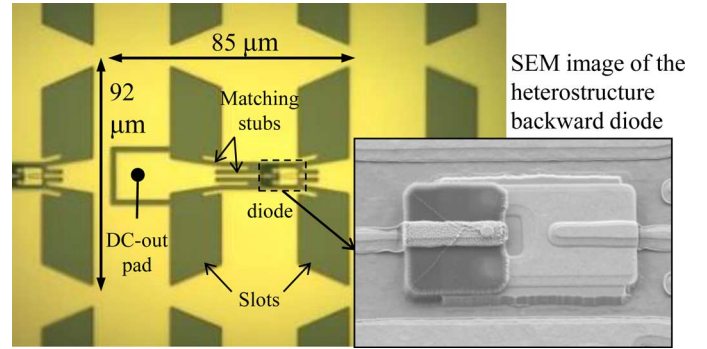

Fig. 3. Layout of the butterfly-shaped broadband antenna operating in the 0.6–1.2 THz range. A DC pad is used for flip-chip bonding to the read-out electronics.

order to tackle the latter, careful antenna/diode coupling is required to ensure maximum power transfer onto the sensor as presented in detail below.

The paper is organized as follows: In Section II, we outline the design process for a broadband FPA covering 0.6–1.2 THz, starting with the broadband slot antenna elements. The antenna design is carried out using a full wave moment method simulation approach capable of accurate characterization of antenna impedance and radiation/reception pattern. Section III presents the quasi-optical modeling of the overall imaging performance of the FPA. In Sections IV and V, we conclude with the validation and characterization of the prototype real-time THz camera.

II. BROADBAND FOCAL PLANE ARRAY DESIGN

Double slot antennas on hemispherical lenses have been very popular due to their performance, versatility, manufacturing simplicity and monolithic integration with semiconductor devices. They consist of an array of two planar slot antennas connected with a co-planar waveguide (CPW) structure [13]. As such, the pattern of the array antenna exhibits a single dominant lobe, directed mostly into the substrate of the hemispherical lens. The shape of the main lobe can be optimized for excellent coupling to the Gaussian-optics of the hemispherical lens and the subsequent objective lens optics. However, since the main radiators are the slot dipoles, these antennas are typically quite narrowband and cannot be readily used for broadband THz sensing. In order to substantially increase the antenna bandwidth without significantly impacting its pattern and Gaussian coupling efficiency requires a careful re-design of the antenna structure. Conventional broadband antennas, such as slot spirals and log-periodic designs are typically larger in size, and thus are not desired for densely-packed FPAs. Broadband dipole-based antenna topologies, as shown in Fig. 3, are more attractive for small size THz pixels that can be integrated into dense-format FPAs.

Bandwidth performance of double slot antennas can be substantially improved by the butterfly-shaped design depicted in Fig. 3. As seen, the widths of the slot dipoles are increased substantially and the dipole tips are tapered to resemble a butterfly's wings. The design modification is also akin to a bowtie antenna, which is known to exhibit wideband performance. The two parameters that determine the final optimal design are the antenna/diode impedance matching and radiation pattern. With the restriction of 100 μm $\times$ 100 μm pixel area, the goal is to achieve optimal conjugate impedance matching
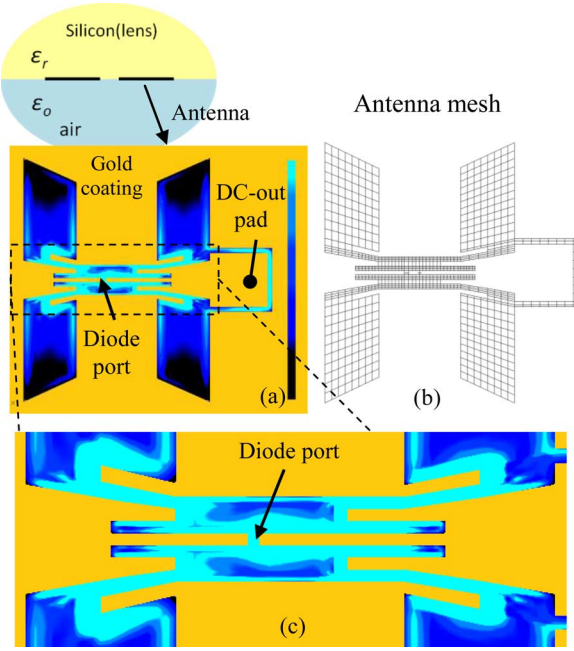
Fig. 4. Butterfly antenna element for the THz FPA (a) magnetic current distribution on the antenna slots at 875 GHz, (b) discretization of the antenna slots with quadrilateral finite elements, and (c) detail of the antenna feed for diode impedance matching.

Fig. 5. Computed butterfly antenna radiation patterns inside the silicon lens (H-plane). The pattern maintains a broadside radiation lobe (8–12 dB) in the 0.6–1.2 THz range. Less than 5% is radiated into the air.

Fig. 6. Computed radiation efficiency in the 0.6–1.2 THz range (inside the semi-infinite silicon lens).

while maintaining a single, stable radiation lobe over a wide bandwidth (0.6–1.2 THz). It is relatively straightforward to design the dual-slot antenna topology that radiates a single lobe over the 0.6–1.2 THz range [14]. Subsequently, we focus on optimizing the antenna input impedance so that it is conjugate-matched to the diode's small signal impedance. This is primarily achieved by tuning the CPW structure connecting the two wings, a process that does not alter the antennas radiation characteristics. Finally, the DC pad separation gap on the side of each antenna is designed to exhibit a very large capacitance at the THz frequencies, thus shorting out and not contributing to antenna impedance or radiation pattern.

The broadband butterfly antenna design is carried out using an in-house full-wave moment method modeling approach based on quadrilateral finite elements and conformal rooftop basis functions [15], as depicted in Fig. 4(b). Since the hemispherical lens is electrically large (many wavelengths in diameter, typically $> 40\lambda$), the planar slot antenna is assumed to lie at the air-substrate boundary and the surface-magnetic current on the antenna aperture is discretized.

The magnetic field surface integral equation (MFIE) formulation was used assuming the half-space Green's function for the lens medium (on top) and the free-space at the bottom half was used [16]. As such, the diode-port impedance of the antenna (shown in Fig. 4(c), as well as the radiation pattern into the dielectric substrate can be calculated accurately. Moreover, since only the antenna slots are discretized, the moment method matrix size is rather small, thus design iterations for impedance tuning can be very efficiently carried out over the wide frequency band.

Fig. 4 shows a typical moment method solution for the magnetic currents on the butterfly antenna arms and the connecting CPW structure. Subsequently, the antenna pattern can also be computed for the desired frequency range, as depicted in Fig. 5.
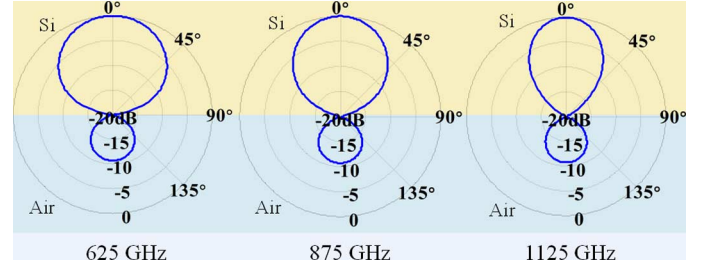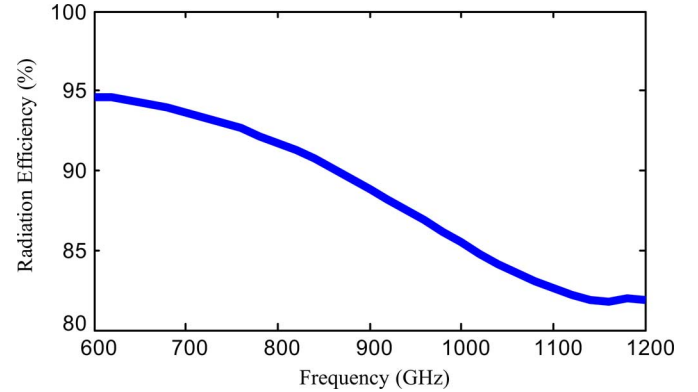
As seen, the antenna pattern exhibits a highly directive main lobe toward the substrate half-space, a much desired property of substrate-integrated slot antennas [12]. The radiation efficiency inside the silicon dome is depicted in Fig. 6. Here the loss of the GaAs substrate is included ($\tan\delta \sim 1.6 \times 10^{-3}$) whereas silicon loss is neglected ($\tan\delta \sim 1.5 \times 10^{-5}$). We note here that the effect of the ROIC has also been carefully investigated. In the actual prototype, the read-out circuit is flip-chipped on the back side of the FPA via indium bumps. Each bump occupies an area of less than $20\,\mu\text{m} \times 20\,\mu\text{m}$, with a bump-height around $15\,\mu\text{m}$. Full-wave simulations have not indicated any significant effect on either antenna input impedance or its radiation performance when the ROIC is situated $15\,\mu\text{m}$ behind the FPA.

In order to most effectively couple the incoming THz radiation onto the sensor element (i.e., the integrated HBD diode), the antenna impedance must be conjugate-matched to the diode's input terminals. Here, we used an equivalent ADS [18] model for the diode impedance. The model was extracted by measurements carried out in the 0–110 GHz range and extrapolated to 0.6–1.2 THz. As such, the current diode features impedance of 80 Ohm constant resistance and 40–70 Ohm capacitive reactance. By carefully designing the CPW geometry in the antenna, as shown in Fig. 4(c), we achieve optimum impedance-matching, maximizing the integrated sensor's responsivity, R_v (which relates the output baseband voltage to incident THz power measured in V/W). The design goal is to transform the typical narrowband double slot antenna impedance, which features rapid fluctuations across the operating bandwidth, into a more uniform performance (see Fig. 7). This is primarily achieved by tapering the antenna slots and making them wider. Additionally, by altering the CPW section
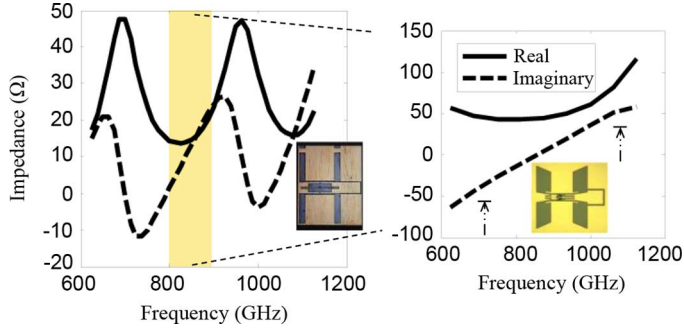
Fig. 7. Broadband antenna impedance design. Left: The impedance of a narrow double slot antenna exhibits intense resonances [17]. Right: The butterfly-shaped broadband antenna features more smooth impedance, closer to the diode's conjugate impedance.

around the antenna feed (by additional matching stubs), we increase the inductance and bring the overall impedance closer to the ideal conjugate value. We note here that for the calculation of both antenna input impedance and radiation pattern only one reflection in the lens/air interface has been considered. As it was studied in [19], for an electrically large hemispherical lens, multiple reflections do not have a significant effect on the antenna performance. Additionally, in a previous work the impedance of a scaled version of the butterfly antenna has been characterized using an indirect measurement method [20]. The results exhibit very good agreement with the computed impedance.

Obviously, achieving the maximum responsivity is of utmost importance for THz sensor performance. Although the antenna-diode impedance match is a key parameter for maximizing the sensor responsivity, this metric is primarily determined by the characteristics and the technology of sensor device itself (HDB diode in our case). Thus, new sensor materials and devices would require a careful redesign of the THz antenna structures to maximize responsivity. In addition to impedance matching considerations, external coupling of incident radiation onto the antenna structure must also be optimized via external quasi-optical lenses and/or reflectors. We next summarize an approximate but effective method for modeling the performance of the quasi-optical components in the THz FPA system. Collimation and coupling of THz waves onto the FPA antennas are considered using first-order high-frequency approximations that are well suited for electrically large lens trains and reflector chains. As such, a hybrid full-wave high-frequency approach is adopted here for concurrently modeling pixel patterns and responsivity as well as the external quasi-optical imaging system. In the following, we consider the analysis of quasi-optical propagation/coupling of THz radiation onto the FPA sensor.

III. QUASI-OPTICAL MODELING OF THE THz FPA IMAGING PERFORMANCE

The butterfly-shaped antenna design outlined above achieves optimal impedance match at the HBD port while exhibiting favorable far-field radiation pattern required for efficient coupling into the quasi-optical imaging system (as illustrated in Fig. 2). The focusing effects of the hemispherical lens are computed using an approximation based on the electrically large dimensions of the hemispherical lens.
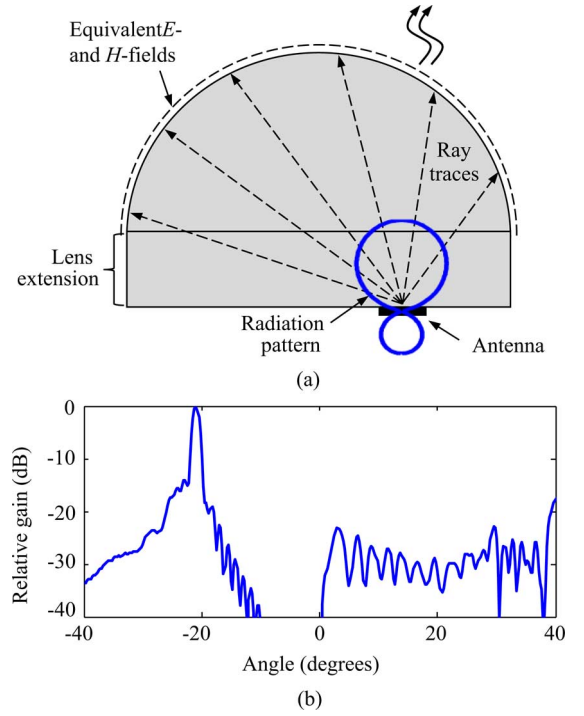

Fig. 8. Computed far-field radiation outside the substrate lens (a) Ray-tracing/ physical optics analysis for the double slot THz antenna radiation pattern in the presence of the hyper-hemispherical lens. (b) Far field pattern (outside the substrate lens) of an antenna placed 1.8 mm off axis at 875 GHz.

The antenna fields and pattern inside the dielectric can be readily computed using the moment method solution for the aperture magnetic currents, as shown in Fig. 5. Using the antenna pattern towards the silicon lens half space, a ray-tracing (or physical-optics) approach can be used to compute the antenna pattern outside the hyper-hemispherical lens [21]. To do so, first, the Fresnel transmission coefficients for all rays emanating from the antenna center and impinging upon the inner surface of the lens are computed, as shown in Fig. 8(a). The total electromagnetic fields radiated by the magnetic currents on the THz antenna slots are also computed on the inner lens surface. Subsequently, these interior field values are multiplied by the corresponding Fresnel transmission coefficients for the associated rays to compute the electromagnetic fields on the outer lens surface. Antenna radiation pattern outside the lens can thus be computed as the far-zone radiation of these outer-surface fields [see Fig. 8(b)].

For example, we illustrate a simple scenario in Fig. 9, where a 31×31 element FPA is considered. For ease of modeling, a radiating FPA is considered and reciprocity is used to calculate receiving properties. As seen, each antenna/pixel radiates a distinct collimated beam propagating out of the hemispherical lens at a corresponding angle with respect to the optical axis. Subsequently, each beam is refracted by the objective lens and collimated on the object plane. The pixelated pattern on the object plane [shown in Fig. 10(a)] corresponds to the receiving pattern of the FPA via reciprocity. In essence, the projection of the beams on the object plane constitutes each pixel's Airy patterns, whose shape and spacing determine the overall THz image quality.

In order to further assess the FPA imaging performance, we considered a 'T'-shaped aperture. By convolving the beam pat-
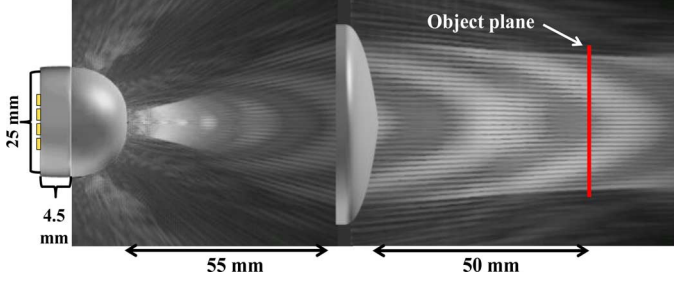
Fig. 9. Computed beam intensity distribution for a 31×31 element FPA illumination. The element beams are projected on object plane.
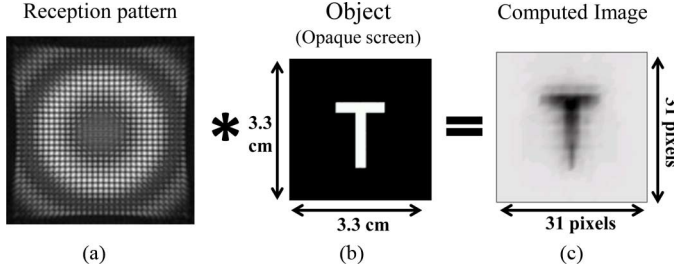

Fig. 10. (a) Computed FPA reception pattern, (b) opaque screen used as object, (c) the expected THz image is computed by convolution of the reception pattern with the object.
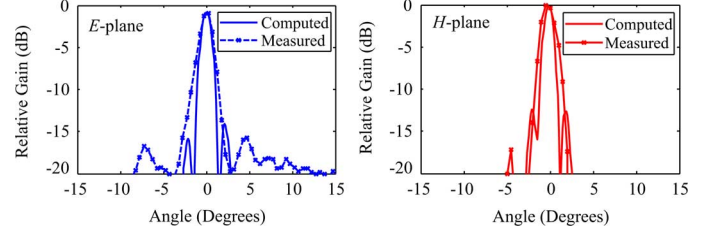

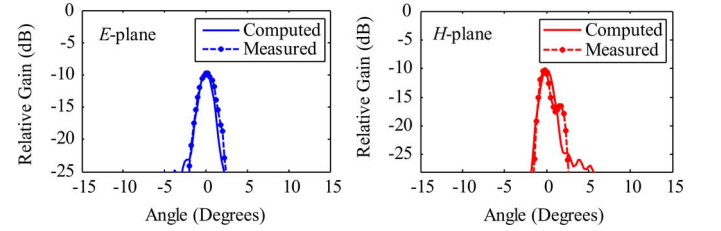Fig. 11. Receiving patterns of an antenna pixel near the optical axis at 700 GHz.

Fig. 12. Receiving patterns of an antenna pixel located off-optical axis (at a position 1.5 mm from x-axis, 1.6 mm from y-axis) at 700 GHz. As expected, gain is reduced significantly and antenna beam-width becomes wider.

tern with the aperture pattern, we can compute the expected THz image projected on the FPA antennas, as illustrated in Fig. 10. In this example, we assume a 1 mm wide 'T'-shaped slot located 50 mm behind the objective lens, as depicted in Fig. 9. In the design process, we assume an objective lens extending infinitely in lateral dimensions. This is clearly justified since the objective lens is under-illuminated (with an edge taper < -10 dB) and thus the edge diffraction effects are minimal.

The hybrid computational modeling approach summarized above provides an effective tool to compute the overall FPA performance by incorporating not only the quasi-optical imaging system but also the antenna characteristics. A series of measurements are presented in the next section, to illustrate the accuracy of the modeling and design process, leading to a prototype THz camera.

IV. CHARACTERIZATION OF FPA RADIATION PATTERNS AND SENSITIVITY

We next demonstrate the performance of the THz FPA camera constructed using the antenna designs presented above. A large-format (80×64 pixel) THz FPA (Fig. 1) was manufactured using the optimized 100 μm-pitch butterfly slot antennas shown in Fig. 3. The FPA was fabricated on a 500 μm thick GaAs substrate ($\varepsilon_r \sim 12.9$) and was placed at the center of a 25 mm-diameter high-resistivity silicon hemispherical lens with a 4 mm extension. A commercial voltage-mode read-out circuit (from New Imaging Technologies, [22]) was integrated through a flip-chip bonding process onto the back side of the FPA plane. The sensitivity as well as the radiation (reception) properties of the FPA pixels was characterized as outlined below.

The radiation patterns of the FPA antennas were measured by recording the DC output voltage on the sensor diode (from the ROIC output) for each plane wave incidence direction. The THz camera was affixed on a motorized precision controlled rotator and was illuminated by a collimated beam (approximating a plane wave). The pattern measurement was collected with a half degree step size on both the E- and H- planes. Figs. 11 and 12 depict the measured and computed receiving patterns for FPA antennas located on and off the optical axis, respectively.

The next set of measurements is focused on characterizing the sensitivity. To do so, the FPA is illuminated using the 5–8 μWatt output of VDI's THz extender [22] as the source. A diagonal horn antenna was used to provide a focused beam onto a single pixel in the FPA, as shown in Fig. 13. However, when observed on the camera monitor, illumination of the neighboring elements is unavoidable. Therefore, optical responsivity is computed by summing the DC voltages of the illuminated pixels and dividing by the incident THz power (provided by VDI specification sheet). Fig. 14 depicts the responsivity values measured with the VDI extender in the 0.6–0.75 THz. Maximum optical responsivity is recorded around 600 V/Watt at 700 GHz. In addition to the VDI extender, a backward wave oscillator (BWO) is used in a similar fashion to extend the measurements up to 0.875 THz. We note that this measurement corresponds to the overall responsivity of the FPA, where the lenses reflections, impedance mismatches and material losses are all included. The electrical responsivity (solid line) which was computed using the diode's circuit model (without including any loss or impedance mismatches) is also shown in Fig. 14.

The other important metric in imaging systems is noise equivalent power (NEP). The NEP was calculated using the measured optical responsivity and sensor voltage noise. The ROIC exhibits noise levels of around 125 μV (or 510 nV/$\sqrt{\text{Hz}}$) at 5 fps acquisition speed, resulting in NEP of 208 nW. For the NEP density calculation, we have to account for the electronics sampling speed. More specifically, the ROIC operated by reading sequentially the voltage from each of the 320×256 pixels, resulting in 850 pW/$\sqrt{\text{Hz}}$ noise density.

Table I compares the performance of our THz camera with other state-of-the-art room temperature FPA technologies.

V. THz IMAGE ACQUISITION

The second set of measurements is focused on validating the overall imaging performance of the THz camera. For this, the

TABLE I
COMPARISON OF VARIOUS ROOM TEMPERATURE THz FPA TECHNOLOGIES

| Type	Pixels	Bandwidth	Responsivity* (optical)	NEP (optical)	Optics	Frame rate	Reference
Sb-HBD	5120 (80×64)	0.6-1 THz	600 V/W 0.7 THz	$850 pW/\sqrt{Hz}$	Silicon lens	100 fps (0.6-1 THz)	This work
CMOS	1024 (32×32)	0.75-1 THz	1130 V/W 0.9THz	$470 pW/\sqrt{Hz}$	Silicon lens	25fps (0.6-1THz)	[11]
CMOS	15 (3×5)	0.65-1 THz	800 V/W 1THz	$66 pW/\sqrt{Hz}$	-	Scanned, 1 THz	[9]
VOx Bolometers	76800 (320×240)	1.1 – 30 THz	-	$0.1 pW/\sqrt{Hz} > 6THz$ $10 pW/\sqrt{Hz}$ 1.1THz	-	60 fps	[24]

*Without amplification
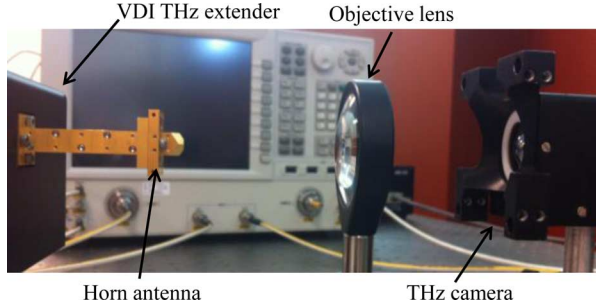
Fig. 13. Quasi-optical setup for responsivity measurement. THz radiation is coupled from the VNA to the FPA with the help of a horn antenna and an objective lens.
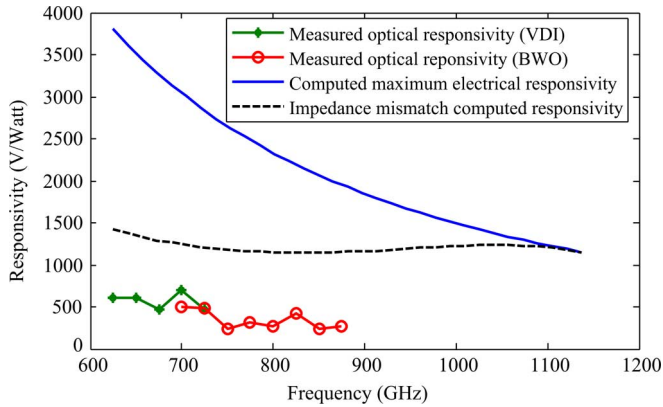

Fig. 14. *Solid line*: Maximum electrical responsivity of an individual FPA pixel (diode depletion area: $0.17\ \mu m^2$). *Dashed line*: diode responsivity including impedance mismatch, and *marked lines*: measured (optical) responsivity.
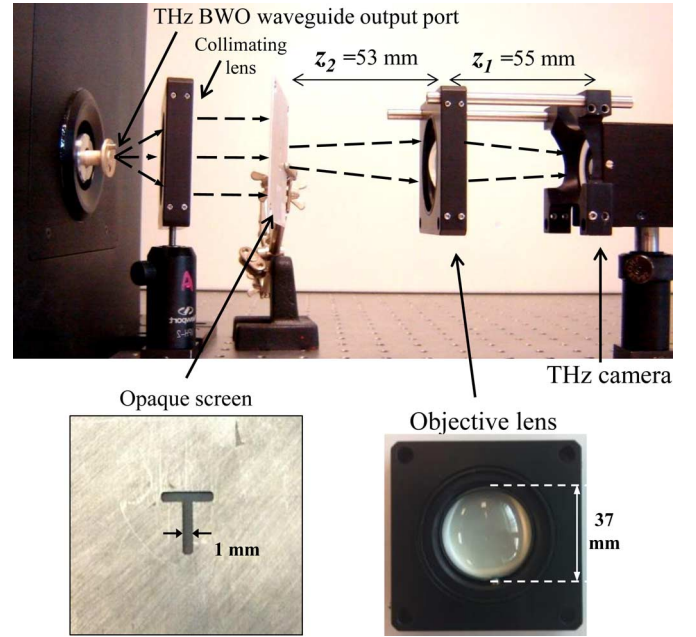

Fig. 15. Reverse microscope configuration setup for THz imaging. A BWO THz source illuminates the object (opaque screen). Part of the THz radiation transmitted through the object is collected by the camera optics and projected on the FPA.
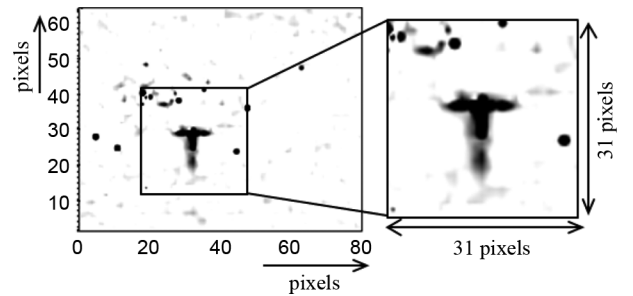
Fig. 16. Recorded THz camera images at 700 GHz. Left: THz image of a 1 mm slot width 'T'. Right: Detail of a 31×31 pixel area of the image.

setup shown in Fig. 15 is considered, where a BWO (with 6 MHz signal bandwidth) is used as the source in conjunction with a collimating lens illuminating the test object with 0.75 mW at 700 GHz. We note here that both the BWO and the FPA antennas are linearly polarized and properly aligned for polarization matching. A metallic opaque screen with a 'T'-shaped slot is used as the test object. The camera consists of an $f/1.35$ objective lens with a 50 mm focal length. Best image quality is achieved by varying the distances between the various components and the resulting configuration is shown in Fig. 15.

The captured snapshot of the T-shaped aperture is shown in Fig. 16 and is in excellent agreement with the computed image in Fig. 10(c). At 700 GHz the wavelength ($\lambda < 0.5$ mm) is still much shorter than the narrowest slot tested (~ 1 mm). Therefore, diffraction is not expected to severely affect the propagation of THz radiation through the slotted aperture. We note here that mainly the central 31×31-pixel area contributes to the

image due to the spread of THz incident power over a wide area and the off axis aberrations resulting from the small size of the hemispherical lens [17] . Moreover, the noticeable noise in the measured pattern is due to the electronic noise introduced by the integrated read-out circuit (dynamic range ~ 24 dB, NEP ~ 208 nW) as well as several "dead"-pixels in the FPA (approximately 1 out of 50).

As a second example, we considered a steel screw inside a mailing envelope to illustrate the penetration of THz waves

Fig. 17. THz image of a steel screw placed inside an envelope. (a) Image of the screw and the envelope (b) BWO source beam trace and (c) THz image of the screw inside the envelope.

through the paper package. The envelope and the dimensions of the steel screw used in standard optical table setups are show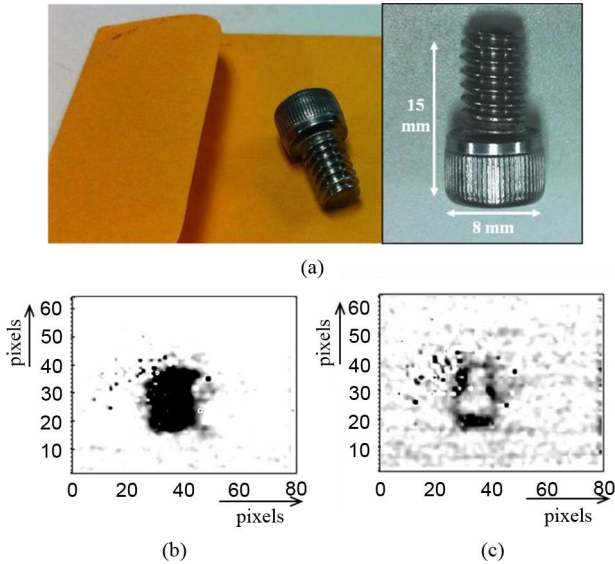n in Fig. 17(a). First, the FPA was illuminated directly by the BWO source as shown in Fig. 17(b) (the pattern seen here is typical for a multi-moded BWO waveguide output). From Fig. 17(c), the steel screw inside the envelope can be clearly seen when the sample is placed between the BWO source and the THz FPA. Compared to the T-shaped slot, illumination area is larger and wave attenuates while propagating through the paper. Therefore, dynamic range decreases to 15 dB.

As noted above, the additional factors that affect the quality of the recorded images are the read-out circuit noise, dead-pixel patterns, and the source illumination pattern. As seen in the recorded images, the noise added from the read-out electronics can be substantial. As mentioned earlier, ROIC reads sequentially the voltages of the 320×256 pixels at a maximum frame rate of 100 fps. This results in a very short integration time per pixel (12 nsec). A 20-frame averaging was used to minimize this electronic noise, resulting in an equivalent 5 fps acquisition speed. Furthermore, due to the multi-moded nature of the BWO output port, a uniform object illumination could not be obtained. The BWO output is a simple open ended rectangular waveguide; however this waveguide is rather large at the BWO frequency and can support multiple modes. Thus, the open waveguide aperture radiates a beam that deviates substantially from a simple Gaussian beam profile, as seen in Fig. 17(b).

VI. Conclusions

We presented the design and characterization of the first broadband real-time HBD-based FPA for THz imaging applications. Broadband planar slot antennas are the building blocks of the FPA, exhibiting both an efficient impedance match with the integrated sensor devices (viz. HBDs) and excellent radiation coupling characteristics. The quasi-optical system was also analyzed using a hybrid moment method-ray-tracing technique allowing for the system-level characterization of the overall imaging performance of the camera. The presented approach demonstrates the synergies between optics and antenna/RF

engineering for beam shaping and impedance matching as an important design method in the THz FPA technology. The prototype FPA realizes a compact (8 mm × 6.4 mm area), planar device which is manufactured with mature fabrication techniques and can be easily integrated (via flip-chip bonding) with standard read-out electronics, providing a cost-effective implementation for a wide variety of THz imaging applications. Furthermore, the measured THz images illustrate that the FPA can resolve sub-millimeter diffraction limited details. Concurrently, measurements using a BWO source demonstrate that the FPA covers a broad frequency range from 0.6–0.9 THz, with a computed upper bound of 1.2 THz.

Our first prototype is obviously not void of some shortcomings. The issue of "dead" pixels can be easily mitigated by scaling up the FPA fabrication process. This first prototype was fabricated as a single wafer and no testing was conducted prior to FPA assembly with the ROIC. To eliminate the dead-pixel problem, burn-in tests need to be implemented to discard faulty FPAs prior to ROIC flip-bonding.

Finally, we note that the imaging area of this prototype FPA is limited to about 31×31 pixels due primarily to the limited output power of the THz source and off axis aberrations of the hemispherical lens. The latter can be substantially mitigated using beam-tilted off axis antennas, presented in a previous study [17]. Beam-tilting in the H-plane can be accomplished by shifting the antenna feed across the radiating slots. A similar effect occurs when the feed is placed closer to one of the slots, tilting the antenna beam in the E-plane. The combination of these "feed displacements" can be used to control the beam direction simultaneously in both E- and H- planes.

References

[1] F. C. De Lucia, "Millimeter and submillimeter-wave spectroscopy," *Molecular Spectroscopy, Modern Res.*, vol. II, pp. 73–92, 1976.

[2] U. A. Khan, N. Al-Moayed, N. Nguyen, K. A. Korolev, M. N. Afsar, and S. P. Naber, "Broadband dielectric characterization of tumorous and nontumorous breast tissues," *IEEE Trans. Microw. Theory Tech.*, vol. 55, no. 12, pp. 2887–2893, Dec. 2007.

[3] P. Ashworth, E. Pickwell-MacPherson, E. Provenzano, S. Pinder, A. Purushotham, M. Pepper, and V. Wallace, "Terahertz pulsed spectroscopy of freshly excised human breast cancer," *Opt. Exp.*, vol. 17, pp. 12444–12454, 2009.

[4] A. Menikh, S. P. Mickan, H. Liu, R. Maccoll, and X. C. Zhang, "Label-free amplified bioaffinity detection using terahertz wave technology," *Biosens. Bioelectron*, vol. 20, no. 3, pp. 658–62, Oct. 2004.

[5] H.-B. Liu, H. Zhong, N. Karpowicz, Y. Chen, and X.-C. Zhang, "Terahertz spectroscopy and imaging for defense and security applications," *Proc. IEEE*, vol. 95, no. 8, pp. 1514–1527, Aug. 2007.

[6] Z. Ze, R. Rajavel, P. Deelman, and P. Fay, "Sub-micron area heterojunction backward diode millimeter-wave detectors with 0.18 $pW/Hz^{1/2}$ noise equivalent power," *IEEE Microw. Wireless Compon. Lett.*, vol. 21, no. 5, pp. 267–269, May 2011.

[7] J. Lusakowski, W. Knap, N. Dyakonova, L. Varani, J. Mateos, T. Gonzalez, Y. Roelens, S. Bollaert, A. Cappy, and K. Karpierz, "Voltage tunable terahertz emission from a ballistic nanometer InGaAs/InAlAs transistor," *J. Appl. Phys.*, vol. 97, p. 064307, 2005.

[8] W. Deal, X. B. Mei, K. M. K. H. Leong, V. Radisic, S. Sarkozy, and R. Lai, "THz monolithic integrated circuits using InP high electron mobility transistors," *IEEE Trans. Terahertz Sci. Technol.*, vol. 1, no. 1, pp. 25–32, Sep. 2011.

[9] R. A. Hadi, H. Sherry, J. Grzyb, N. Baktash, Y. Zhao, E. Ojefors, A. Kaiser, A. Cathelin, and U. Pfeiffer, "A broadband 0.6 to 1 THz CMOS imaging detector with an integrated lens," in *Proc. Microw. Symp. Digest (MTT), 2011 IEEE MTT-S Int.*, Jun. 5–10, 2011, pp. 1–4.

[10] S. Boppel, A. Lisauskas, V. Krozer, and H. G. Roskos, "Towards monolithically integrated CMOS cameras for active imaging with 600 GHz radiation," *Proc. SPIE 8261, Terahertz Technol. Applicat. V*, vol. 826106, 2012.

[11] J. Grzyb, H. Sherry, Y. Zhao, R. Al Hadi, A. Cathelin, A. Kaiser, and U. Pfeiffer, "Real-time video rate imaging with a 1 k-pixel THz CMOS focal plane array," *Proc. SPIE*, vol. 8362, pp. 83620C–83620C-12, 2012.

[12] D. F. Filipovic, S. S. Gearhart, and G. M. Rebeiz, "Double-slot antennas on extended hemispherical and elliptical silicon dielectric lenses," *IEEE Trans. Microw. Theory Tech.*, vol. 41, no. 10, pp. 1738–1749, Oct. 1993.

[13] D. B. Rutledge, D. P. Neikirk, and D. P. Kasilingram, "Integrated circuit antennas," in *Infrared and Millimeter-waves*, K. Button, Ed. New York, NY, USA: Academic, 1983, vol. 10, pp. 1–90.

[14] G. C. Trichopoulos, K. Topalli, and K. Sertel, "Imaging performance of a THz focal plane array," in *Proc. Antennas Propag. (APSURSI), 2011 IEEE Int. Symp.*, Jul. 3–8, 2011, pp. 134–136.

[15] K. Sertel and J. L. Volakis, "Method of moments solution of volume integral equations using parametric geometry modeling," *Radio Sci.*, vol. 37, no. 1, pp. 10–17, 2002.

[16] G. V. Eleftheriades and G. M. Rebeiz, "Self and mutual admittance of slot antennas on a dielectric half-space," *J. Infrared Millimeter Waves*, vol. 14, no. 10, pp. 1925–1946, Jul. 1993.

[17] G. C. Trichopoulos, G. Mumcu, K. Sertel, H. L. Mosbacker, and P. Smith, "A novel approach for improving off axis pixel performance of terahertz focal plane arrays," *IEEE Trans. Microw. Theory Tech.*, vol. 58, no. 7, pp. 2014–2021, Jul. 2010.

[18] Advanced Design System (ADS), Agilent Technologies Inc..

[19] M. J. M. van der Vorst, P. J. I. de Maagt, A. Neto, A. L. Reynolds, R. M. Heeres, W. Luinge, and M. H. A. J. Herben, "Effect of internal reflections on the radiation properties and input impedance of integrated lens antennas-comparison between theory and measurements," *IEEE Trans. Microw. Theory Tech.*, vol. 49, no. 6, pp. 1118–1125, Jun. 2001.

[20] K. Topalli, G. C. Trichopoulos, and K. Sertel, "An indirect impedance characterization method for monolithic THz antennas using coplanar probe measurements," *IEEE Antennas Wireless Propag.*, vol. 11, pp. 3–5, 2012.

[21] R. E. Collin, *Antennas and Radiowave Propagation*. New York, NY, USA: McGraw-Hill, 1985, ch. 4.

[22] New Imaging Technologies, 1–4 Impasse de la Noisette, Bat D, 1er Etage, 91370,. Verrières-le-Buisson, France [Online]. Available: http://www.new-imaging-technologies.com

[23] Virginia Diodes Inc..

[24] N. Oda, "Uncooled bolometer-type terahertz focal plane array and camera for real-time imaging," *Comptes Rendus Phys., ISSN 1631-0705*, vol. 11, no. 7–8, pp. 496–509, Aug.–Oct. 2010.

H. Lee Mosbacker received the B.S. degree in physics from Honors Tutorial College, Ohio University, Athens, OH, USA, in 1999. In 2008, he received the Ph.D. degree in physics from The Ohio State University, Columbus, OH, USA.

From 2000 to 2002, he worked as a programmer analyst at Nationwide Financial developing market timing applications for mutual fund managers. Since 2007, Lee has been the Chief Technology Officer of Traycer Diagnostic Systems, where he has been involved in the scientific and technical aspects of growing an early-stage technology company, including grant and fund raising and the conceptualization and development of microwave and terahertz frequency detection arrays. In 2005, Lee co-founded Techriculture, a non-profit that helps inventors and scientists in early stage product ideation and prototype development through educational, networking, technical, and financial consulting.

Don Burdette received the Ph.D. degree in physics from The Ohio State University, Columbus, OH, USA, where his dissertation research involved the design and testing of a prototype small animal PET medical imaging scanner that can operate in strong magnetic fields.

During the concept stage, he wrote detailed physics simulations in order to determine the optimal detector geometry and to characterize the expected system performance. He performed simulations, designed the mechanics of the apparatus, supervised the manufacturing process, tested the prototype device, and aided in the development of advanced 3-D reconstruction software. He has contributed to the development and testing of various other imaging system prototypes including the Compton Camera, Compton PET, and the Beta Probe in collaboration with the University of Michigan, CERN, Univerity of Ljubljana, University of Valencia, University of Perugia, and the Wright Center of Biomedical Innovation. He has authored or co-authored multiple articles on imaging component and system development in leading scientific journals.

Kubilay Sertel received the Ph.D. degree in 2003 from the Electrical Engineering and Computer Science Department, University of Michigan-Ann Arbor, MI, USA.

He is currently an Assistant Professor at the Electrical and Computer Engineering Department at the Ohio State University, Columbus, OH, USA. He was a Research Scientist at the ElectroScience Laboratory and an Adjunct Professor at the Electrical and Computer Engineering Department at the Ohio State University during 2003–2012. His current research focuses on the analysis and design of THz and mmW sensors, antennas arrays and spectroscopy systems for biomedical and non-destructive imaging, as well as ultra wideband low-profile antennas and phased arrays for cognitive sensing and opportunistic wireless networks, reconfigurable antennas, arrays and miniaturization techniques, novel RF materials, frequency selective surfaces/volumes and magneto-dielectric metamaterials, measurement and characterization of anisotropic composites. His expertise also includes applied electromagnetic theory and computational electromagnetics, particularly, curvilinear fast multipole modeling of hybrid integral equation/finite element systems and efficient solution of large-scale, real-life problems on massively parallel supercomputing platforms. He co-authored two books *Frequency Domain Hybrid Finite Element Methods in Electromagnetics* (Morgan & Claypool, 2006), and *Integral Equation Methods for Electromagnetics* (SciTech Publishing, 2012), and published over 50 journal papers and over 170 conference articles.

Prof. Sertel is an elected member of URSI Commission B, and member of Applied Computational Electromagnetics Society.

Georgios C. Trichopoulos was born on April 16, 1981 in Agrinio, Greece. He received the Diploma degree in electrical and computer engineering from Democritus University of Thrace, Greece, 2004, and the M.S. degree in biomedical engineering from National Technical University of Athens and University of Patras, Greece (joint program) in 2006. Currently, he is pursuing the Ph.D. degree in electrical engineering at The Ohio State University, Columbus, OH, USA, and he is a Graduate Research Associate at the ElectroScience Laboratory.

His current research interests include electromagnetic theory, terahertz imaging, THz and mmW sensors, and antenna arrays for medical and non-destructive imaging.